








Cite this: *Biomater. Sci.*, 2023, **11**, 2372

## Absorption rate governs cell transduction in dry macroporous scaffolds†

Madelyn VanBlunk, <sup>a,c</sup> Vishal Srikanth, <sup>b</sup> Sharda S. Pandit, <sup>a,c</sup>  
Andrey V. Kuznetsov <sup>b,c</sup> and Yevgeny Brudno <sup>\*a,c,d</sup>

Developing the next generation of cellular therapies will depend on fast, versatile, and efficient cellular reprogramming. Novel biomaterials will play a central role in this process by providing scaffolding and bio-active signals that shape cell fate and function. Previously, our lab reported that dry macroporous alginate scaffolds mediate retroviral transduction of primary T cells with efficiencies that rival the gold-standard clinical spinoculation procedures, which involve centrifugation on Retronectin-coated plates. This scaffold transduction required the scaffolds to be both macroporous and dry. Transduction by dry, macroporous scaffolds, termed “Drydux transduction,” provides a fast and inexpensive method for transducing cells for cellular therapy, including for the production of CAR T cells. In this study, we investigate the mechanism of action by which Drydux transduction works through exploring the impact of pore size, stiffness, viral concentration, and absorption speed on transduction efficiency. We report that Drydux scaffolds with macropores ranging from 50–230 μm and with Young’s moduli ranging from 25–620 kPa all effectively transduce primary T cells, suggesting that these parameters are not central to the mechanism of action, but also demonstrating that Drydux scaffolds can be tuned without losing functionality. Increasing viral concentrations led to significantly higher transduction efficiencies, demonstrating that increased cell–virus interaction is necessary for optimal transduction. Finally, we discovered that the rate with which the cell–virus solution is absorbed into the scaffold is closely correlated to viral transduction efficiency, with faster absorption producing significantly higher transduction. A computational model of liquid flow through porous media validates this finding by showing that increased fluid flow substantially increases collisions between virus particles and cells in a porous scaffold. Taken together, we conclude that the rate of liquid flow through the scaffolds, rather than pore size or stiffness, serves as a central regulator for efficient Drydux transduction.

Received 27th October 2022,  
Accepted 12th January 2023

DOI: 10.1039/d2bm01753a

rsc.li/biomaterials-science

## Introduction

Biomaterials hold exceptional promise for the manufacturing and delivery of cellular therapeutics due to their biocompatibility and tunable mechanical properties, degradation rate, charge, and microstructure.<sup>1–6</sup> Current applications of biomaterial hydrogels and scaffolds include tissue engineered constructs,<sup>3,7,8</sup> drug delivery depots,<sup>9,10</sup> and vehicles for cellular proliferation, differentiation, and delivery.<sup>3,11,12</sup>

Biomaterial scaffolds made from sodium alginate hold promise as delivery vehicles and 3-D structures to organize cells. Alginate is advantageous for its low cost, gelation under physiological conditions, and broad biocompatibility.<sup>3,13–15</sup> Additionally, alginate is classified as Generally Recognized as Safe (GRAS) by the FDA and can be readily obtained and modified with GMP-compliance.<sup>3,13–16</sup> Alginate biomaterials have easily tunable rheological properties, pore size, pore interconnectivity, and compressive strength, which can impact cell proliferation, differentiation, and viability.<sup>3,7,13</sup>

In the past few years, significant attention has focused on biomaterials that improve Chimeric Antigen Receptor (CAR) T cell therapy, a revolutionary anti-cancer treatment with dramatic impact in leukemia and lymphoma and promise for treating solid tumors.<sup>17–21</sup> CAR T cells have an antigen recognition domain that specifically targets a tumor-associated antigen, enabling CAR T cells to recognize and kill tumor cells in the body.<sup>18–20</sup> In the space of CAR T cell therapy, biomaterials have demonstrated utility in improving T cell

<sup>a</sup>Joint Department of Biomedical Engineering, University of North Carolina at Chapel Hill and North Carolina State University, USA. E-mail: ybrudno@ncsu.edu

<sup>b</sup>Department of Mechanical and Aerospace Engineering, North Carolina State University, USA

<sup>c</sup>Comparative Medicine Institute, North Carolina State University, USA

<sup>d</sup>Lineberger Comprehensive Cancer Center, University of North Carolina at Chapel Hill, USA

† Electronic supplementary information (ESI) available: Supplemental Fig. 1–7. See DOI: <https://doi.org/10.1039/d2bm01753a>

activation,<sup>22–25</sup> mediating viral T cell transduction,<sup>11,22,26,27</sup> promoting CAR T cell expansion,<sup>11,25,26,28–30</sup> and releasing CAR T cells in a controlled manner.<sup>11,25</sup>

Recently, our lab reported that dry, macroporous alginate scaffolds, known as “Drydux” scaffolds, mediate retroviral transduction of difficult to transduce primary T cells as efficiently as the gold-standard “spinoculation” for CAR T cell generation: centrifugation of activated T cells and virus on Retronectin-coated plates.<sup>31,32</sup> Drydux scaffolds can enhance cell therapies by offering a logistically simpler and cheaper method for transducing cells than spinoculation. In preliminary efforts to understand the mechanism underpinning Drydux transduction, we demonstrated that cell transduction fails in both dry nanoporous scaffolds and wet macroporous scaffolds, suggesting that scaffold pore size and hygroscopy play central roles in the transduction mechanism.<sup>26</sup>

In this paper, we further define the mechanism behind Drydux transduction by delineating the impact of scaffold pore size, stiffness, viral concentration, seeding volume, and absorption rate on transduction of human primary T cells. We synthesized macroporous alginate scaffolds with varying physical properties by changing the alginate concentration, calcium concentration, and freezing temperature. Within the explored ranges, we found that pore size had some, but unpredictable impact on transduction, while stiffness did not have any impact on transduction. As expected, diluting the virus reduced transduction efficiency. Surprisingly, reducing the volume seeded onto the scaffold, without changing concentration, significantly improved cell transduction. We found that seeded volume and transduction efficiency are both well correlated to the absorption rate, defined as the time needed for the liquid droplet to fully absorb into the scaffold. Taken together, our data indicates that the rate of absorption for the cell–virus solution likely governs Drydux transduction, suggesting specific ways to optimize Drydux scaffolds in future studies.

## Experimental methods

### Preparation of macroporous alginate scaffolds

Scaffolds were prepared as reported previously.<sup>11,26,33</sup> A solution of ultrapure alginate (Pronova, MVG) in deionized (DI) water was vigorously mixed with an equal volume of calcium-D-gluconate solution in DI water for 15 min. Final mixture alginate concentrations ranged from 0.5% to 2% and calcium-D-gluconate concentrations ranged from 0.1% to 0.3%. The resulting mixture was cast 1 mL per well in a 24-well plate and frozen overnight. Freezing temperatures ranged from  $-20$  °C to  $-80$  °C. All frozen scaffolds were lyophilized for 72 h. Scaffolds were stored at 4 °C until used.

### Viral titer and MOI determination

Viral titer was determined by standard flow-cytometry assay.<sup>34</sup> Serially diluted viral stocks were added to HEK293T cells. HEK293T cells were acquired from UNC Lineberger Cancer

Center Tissue Culture Facility. GFP expression was analyzed using flow cytometry 48 h later, and populations with 10–20% GFP<sup>+</sup> cells were used to calculate viral titer. The following equation was used to calculate titer: titer (TU mL<sup>-1</sup>) = (cell number used for infection × percentage of GFP<sup>+</sup> cells)/(virus volume used for infection in each well × dilution fold). MOI was calculated as the ratio of transducing viral particles to number of activated T cells. MOI values of 0.25 to 4 were tested using  $0.5 \times 10^6$  activated T cells to determine which MOI would give a transduction efficiency around 60%. Varying volumes of GFP viral stock were concentrated and mixed with  $0.5 \times 10^6$  activated primary T cells and seeded on top of dry macroporous alginate scaffolds. Scaffolds were incubated in 1 mL complete cell culture media (45% Click's medium (Irvine Scientific), 45% RPMI-1640, 10% HyClone fetal bovine serum (GE Healthcare), 2 mmol L<sup>-1</sup> GlutaMax (Gibco), penicillin (100 units mL<sup>-1</sup>), and streptomycin (100 mg mL<sup>-1</sup>; Gibco)) supplemented with IL-7 (PeproTech, 5 ng mL<sup>-1</sup>) and IL-15 (PeproTech, 10 ng mL<sup>-1</sup>) for 72 h. After 72 h, scaffolds were dissolved with 1 mL of 0.25 M EDTA. Cells were isolated and washed twice with PBS before being analyzed for GFP expression using flow cytometry.

### Scanning electron microscopy

Dry macroporous alginate scaffolds were coated with 70 nm AuPd (Au: 60%, Pd: 40%) for 5 min at 7 nm min<sup>-1</sup> and analyzed on Hitachi SU-3900 variable pressure SEM. Pore sizes were quantified using ImageJ to analyze the SEM images with a minimum of 10 pores measured per scaffold.

### Compression testing

Dry macroporous alginate scaffolds were compressed using Instron 5944. Scaffolds were compressed with a 50 N force at a ramp rate of 0.1 mm s<sup>-1</sup>. Force (N) and displacement (mm) was recorded every 100 ms. Stress was calculated using the equation: force/cross-sectional area. Cross-sectional area was determined using ImageJ to analyze images of each scaffold. Strain was calculated using the equation: displacement/initial length. Initial length was determined using ImageJ to analyze images of each scaffold. The Young's modulus was calculated by calculating the slope of the stress–strain curves in the linear regions before the point of inflection.<sup>35</sup>

### Drydux transduction of activated T cells

GFP retroviral supernatant ( $5 \times 10^6$  TU mL<sup>-1</sup>) was concentrated using Amicon centrifugation filters (MWCO 100 kDa, Millipore) at 1500g for 10 min in a swinging bucket rotor. Concentrated retrovirus ( $2 \times 10^6$  TU in 100  $\mu$ L) was mixed with  $1 \times 10^6$  activated primary T cells (MOI = 2) suspended in 50  $\mu$ L complete cell culture media and pipetted onto the top of the dry macroporous alginate scaffolds. Seeded scaffolds were incubated for 45 min, after which 1 mL of complete cell culture media supplemented with IL-7 (PeproTech, 5 ng mL<sup>-1</sup>) and IL-15 (PeproTech, 10 ng mL<sup>-1</sup>) was added to each scaffold. After 72 h of incubation, scaffolds were dissolved with 1 mL of 0.25 M EDTA. Cells were isolated and washed twice with PBS

before being analyzed for GFP expression using flow cytometry.

### Absorption rate and volumetric flux

Different volumes of activated T cells and concentrated GFP-encoding retroviral supernatant were mixed, keeping a constant MOI of 2. Seeding of this mixture onto the scaffolds was filmed. The absorption rate was calculated as the liquid volume divided by the time it took for the entire droplet to absorb into the scaffold based on there being no liquid visible on top of the scaffold. Volumetric flux was calculated by dividing the absorption rate by the area of the scaffold wetted by the droplet when viewed from the top of the scaffold.

### Cell lines

Primary human T cells were obtained from the peripheral blood of a healthy donor. Primary T cells were isolated from a buffy coat (Gulf Coast Regional Blood Center) using Lymphoprep medium (Accurate Chemical and Scientific Corporation) and frozen in freeze media (50% HyClone fetal bovine serum (GE Healthcare), 40% RPMI-1640, 10% DMSO (Sigma)) until needed. Cells were thawed, resuspended in 9 mL complete media, and centrifuged at 400g for 5 min to remove DMSO. T cells were activated on plates coated with 1  $\mu\text{g mL}^{-1}$  of CD3 (Miltenyi Biotec, 130-093-387, clone OKT-3) and CD28 (BD Biosciences, 555725, clone CD28.2) agonistic monoclonal antibodies. GFP encoded retrovirus was prepared according to previously reported methods.<sup>36</sup> All cells were maintained at 37 °C with 5% CO<sub>2</sub> and 95% humidity.

### Flow cytometry

All samples were analyzed using BD LSRII with a minimum of 10 000 events acquired per sample. Cells were gated on viable cells, FSC singlets, and GFP positive cells [ESI Fig. 1†]. BD FACS Diva 8.0.1 software was used for analysis.

### Statistical analysis and Spearman correlation

All statistical analysis was done using one-way ANOVA or two-way ANOVA with Tukey correction or unpaired *t*-test with

Welch's correction using GraphPad Prism 9. The specific test used and precise *p*-values are noted in individual figures. Spearman correlations were calculated using GraphPad Prism 9 with *r*-values and *p*-values noted in individual figures. \* indicates *p* < 0.0001 with all other *p*-values < 0.05 indicated on plot.

## Results

### Scaffold fabrication

Macroporous scaffolds were fabricated through cryogelation<sup>26,33</sup> [Fig. 1]. Briefly, an equal volume of calcium and alginate solutions were vigorously mixed and cast into wells of a 24-well plate. Samples were then frozen and lyophilized to create dry macroporous alginate scaffolds, which we refer to as "Drydux" scaffolds.

### MOI calibration

Our prior publication reported conditions for excellent transduction efficiencies of 85–95%.<sup>26</sup> However, we were concerned that these high efficiencies could hide small improvements during scaffold optimization. We therefore titrated the multiplicity of infection (MOI) of GFP-encoding gamma-retrovirus to achieve a transduction efficiency of below 60% against primary T cells isolated from human peripheral blood (Gulf Coast Regional Blood Center), reasoning that incremental improvements would be observed more easily by doing so. As expected, lowering the MOI led to a reduction of transduction percent [ESI Fig. 2†]. An MOI of 2, producing 59% transduction efficiency, was determined to be optimal and used for all following experiments unless indicated otherwise.

### Pore size, but not stiffness, is correlated with Drydux transduction efficiency when varying alginate and calcium concentrations

To assess whether calcium or alginate concentration impacted Drydux transduction, we formulated scaffolds with varying calcium (0.1%, 0.2%, 0.3%) and alginate (0.5%, 1.0%, 1.5%, 2.0%) concentrations. Due to instant gelation, scaffolds with 0.3% calcium and 0.5% alginate could not be produced. The

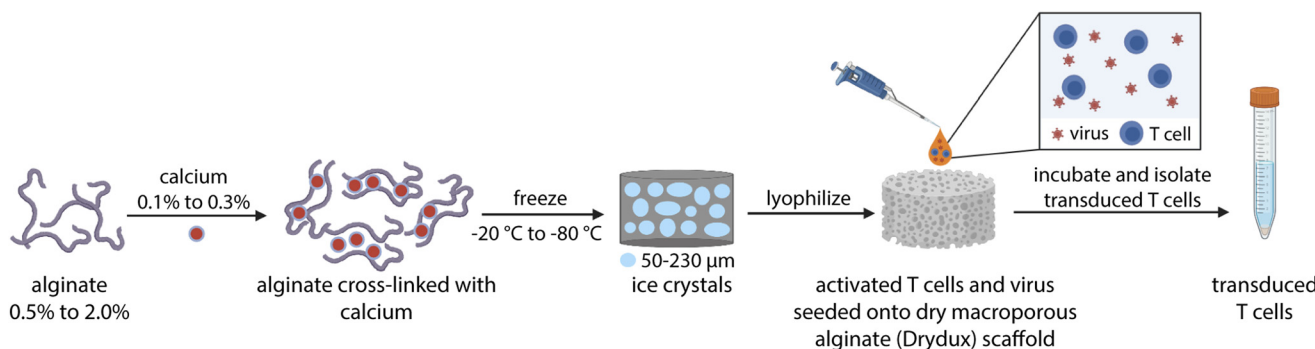


**Fig. 1** Fabrication of dry macroporous alginate (Drydux) scaffolds. An alginate solution is cross-linked with a calcium solution and the resulting gel is frozen overnight followed by lyophilization for 72 h to create dry macroporous scaffolds. Activated T cells and viral particles are mixed and seeded on top of the scaffold and scaffolds are incubated at 37 °C, 5% CO<sub>2</sub>. EDTA is used to dissolve the scaffolds and isolate the transduced T cells.

scaffolds had a cross-sectional area of  $\sim 1.72 \text{ cm}^2$  and a height of  $\sim 5.37 \text{ mm}$  [Fig. 2A]. All the scaffolds produced transduction efficiencies above 50%, indicating the scaffolds were highly capable of transducing cells [Fig. 2B]. Scaffolds made with 0.1% calcium had significantly higher transduction efficiencies than those made with 0.2% and 0.3% calcium. Scaffolds made with 0.5% alginate showed significantly lower transduction than almost all other alginate concentrations, likely due to the lack of surface porosity of the 0.5% alginate scaffolds compared to the other scaffolds. The average pore size of these scaffolds ranged from 76–230  $\mu\text{m}$  [Fig. 2C] and fitting a Spearman correlation indicated there was a strong and significant ( $p = 0.0065$ ) correlation between pore size and transduction efficiency [Fig. 2D].

To determine scaffold stiffness, we submitted Drydux scaffolds to compression testing with a 50 N force and compression rate of  $0.1 \text{ mm s}^{-1}$ . The Young's moduli were calculated based on stress–strain curves generated from compression testing [ESI Fig. 3†]. Scaffolds with 0.1% calcium were softer than scaffolds with 0.2% and 0.3% calcium, and an alginate concentration of 1.5% formed the stiffest scaffolds [Fig. 2E]. There was not a significant ( $p = 0.3510$ ) Spearman correlation between the Young's modulus of the scaffold and transduction efficiency [Fig. 2F].

#### Neither pore size nor stiffness is correlated with Drydux transduction efficiency when varying alginate concentrations and freezing temperature

Several groups have reported that the freezing temperature during cryogelation determines pore size of cryogels.<sup>7,37</sup> To further evaluate the impact of pore size, without the complication of changing crosslinked concentration, we evaluated how changing the freezing temperature impacts scaffold pore size and stiffness and further evaluated whether these changes impact transduction efficiency. Scaffolds were again synthesized using cryogelation with varying alginate concentrations (0.5%, 1.0%, 1.5%, 2.0%), but with a constant calcium concentration of 0.2%, in line with previous reports.<sup>11,26</sup> Scaffolds were then frozen at  $-20 \text{ }^\circ\text{C}$ ,  $-40 \text{ }^\circ\text{C}$ ,  $-60 \text{ }^\circ\text{C}$ , or  $-80 \text{ }^\circ\text{C}$  and lyophilized. The scaffolds had a cross-sectional area of  $\sim 1.78 \text{ cm}^2$  and a height of  $\sim 4.86 \text{ mm}$  [Fig. 3A]. All the scaffolds showed transduction efficiencies above 60%, indicating all the scaffolds successfully transduced cells [Fig. 3B]. As observed above, scaffolds with 0.5% alginate showed significantly worse transduction efficiency than scaffolds made at the other alginate concentrations. There was no significant difference between the 1.0%, 1.5%, and 2.0% alginate concentration scaffolds. Scaffolds frozen at  $-40 \text{ }^\circ\text{C}$  and  $-80 \text{ }^\circ\text{C}$  displayed no significant difference in transduction, but both demonstrated significantly higher transduction than scaffolds frozen at  $-20 \text{ }^\circ\text{C}$  and  $-60 \text{ }^\circ\text{C}$ . The average pore size of these scaffolds ranged from 52–131  $\mu\text{m}$  [Fig. 3C]. In contrast to the results shown in Fig. 2, fitting a Spearman correlation did not produce any significant ( $p = 0.6669$ ) correlation between pore size and transduction efficiency in this experiment [Fig. 3D].

Drydux scaffolds were compressed with a 50 N force and compression rate of  $0.1 \text{ mm s}^{-1}$  to determine scaffold stiffness. The Young's moduli were calculated based on stress–strain curves generated from compression testing [ESI Fig. 4†]. Slower freezing rates generally led to stiffer scaffolds, and scaffolds with 1.0% and 1.5% alginate concentrations formed the stiffest scaffolds [Fig. 3E]. There was no significant ( $p = 0.5938$ ) Spearman correlation between the Young's modulus of the scaffold and transduction efficiency [Fig. 3F].

#### Both viral concentration and seed volume significantly correlate to Drydux transduction efficiencies

Since Drydux transduction did not appear to depend on stiffness and had an unpredictable relationship with pore size, we sought out other factors that might influence transduction efficiency. Viral transduction relies on interactions between virus and cells, so we reasoned that higher viral concentrations should lead to higher transduction efficiency. We suspended 50 000 primary human T cells and 100 000 gamma retrovirus particles in 25  $\mu\text{L}$ , 50  $\mu\text{L}$ , 100  $\mu\text{L}$ , or 200  $\mu\text{L}$  and evaluated Drydux transduction of these solutions. As expected, diluting the virus significantly reduced transduction, confirming our hypothesis [ESI Fig. 5†].

When performing the previous experiment, we noted that larger volumes needed significantly more time to absorb into the scaffold [Fig. 4A and ESI Fig. 6†]. We wondered whether solution volume, and thereby absorption rate, could impact Drydux transduction. To explore this possibility, we evaluated transduction of primary human T cells by retrovirus at a constant concentration with different solution volume (10  $\mu\text{L}$ , 25  $\mu\text{L}$ , 50  $\mu\text{L}$ , 100  $\mu\text{L}$ , or 200  $\mu\text{L}$ ) [Fig. 4B]. At the same time, we measured the speed of liquid absorption into the scaffolds by filming the absorption process and measuring the time it took for the volume to completely absorb into the scaffold. There was a clear trend in transduction efficiency, with smaller seed volumes producing significantly higher transduction efficiencies [Fig. 4C]. In addition, there was a clear trend in absorption rate, with smaller seed volumes translating to faster absorption rates [Fig. 4D]. Fitting a Spearman correlation to the data, we discovered a strong and significant correlation ( $p < 0.0001$ ) between the absorption rate and transduction efficiency of the scaffolds [Fig. 4E]. Since different seed volumes had different absorption areas, determined as the area of the scaffold wetted by the droplet when viewing the top of the scaffold [Fig. 4B], the volumetric flux was calculated by dividing the absorption rate by the absorption area [Fig. 4F]. As expected, we discovered a strong and significant Spearman correlation ( $p < 0.0001$ ) between volumetric flux and transduction [Fig. 4G].

From these results, we concluded that smaller seed volumes absorb into the scaffold faster, leading to increased volumetric flux and higher transduction efficiencies. From this, it stands to reason that spreading the cell–virus solution over a larger surface area would lead to faster absorption and increased transduction. To test this hypothesis, we created scaffolds with cross sectional areas of  $\sim 8.12 \text{ cm}^2$  using 6-well plates and seeded solutions containing 4000 cells per  $\mu\text{L}$



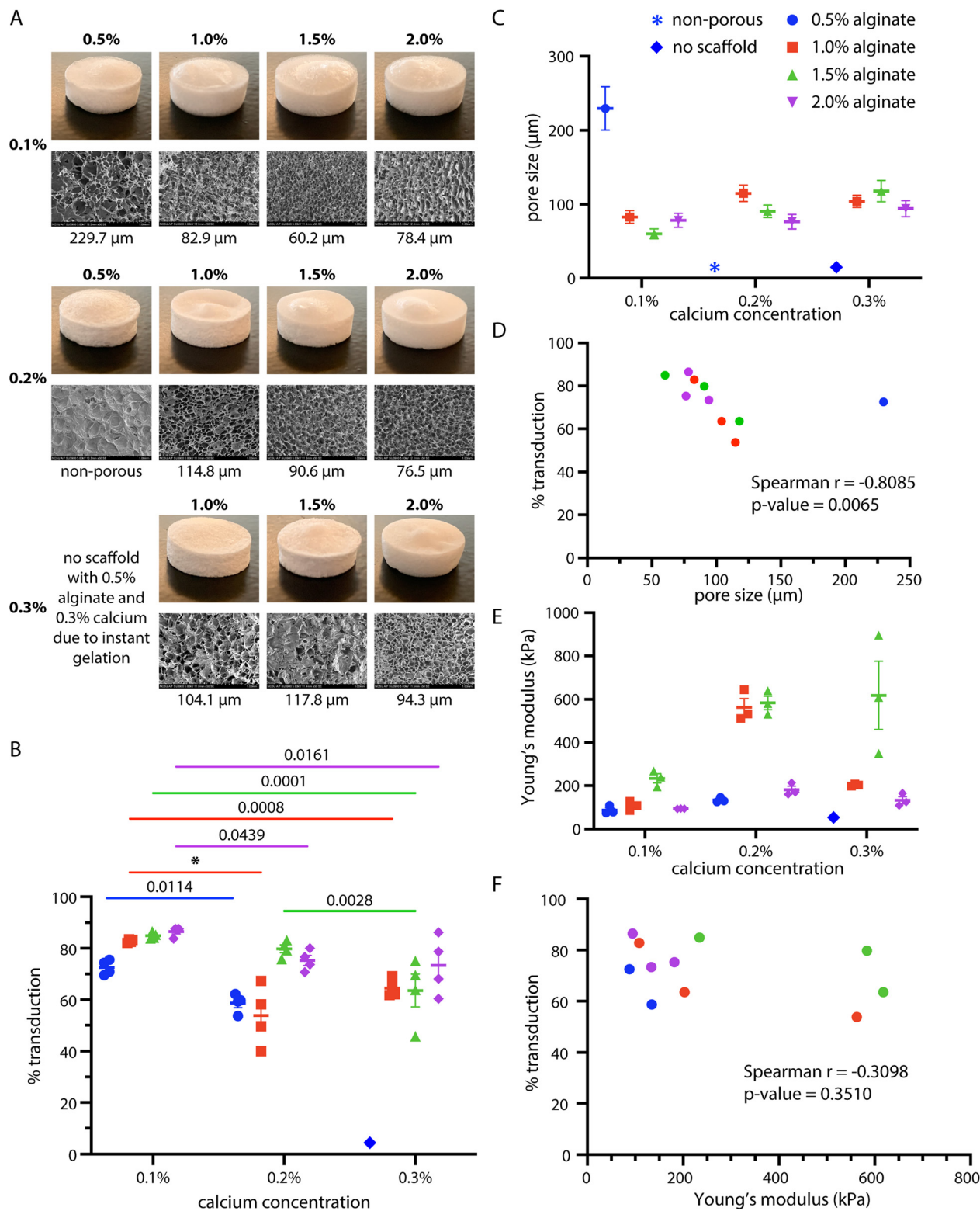


**Fig. 2** Impact of porosity and stiffness on Drydux transduction efficiency varying calcium and alginate concentrations. (A) Photographs of scaffolds with corresponding SEM images and average pore sizes. (B) Quantification of retrovirus transduction efficiency against primary human T cells for each calcium-alginate combination with significance shown between differing calcium concentrations; \* $p < 0.0001$  with all other  $p$ -values  $< 0.05$  indicated on plot; concentrations used were  $\sim 5000$  cells per  $\mu\text{L}$  and  $\sim 10\,000$  viruses per  $\mu\text{L}$ ;  $n = 3$  scaffolds per group; two-way ANOVA with Tukey correction used to determine significance. See ESI Fig. 3† for significance between differing alginate concentrations. (C) Quantification of scaffold pore size using a minimum of 10 pores per scaffold. (D) Spearman correlation between scaffold pore size and transduction efficiency. (E) Quantification of Young's modulus of each scaffold;  $n = 3$  scaffolds per group. (F) Spearman correlation between scaffold stiffness and transduction efficiency. Data are represented as the mean  $\pm$  SEM. Statistical analysis was not completed for (C) or (E).

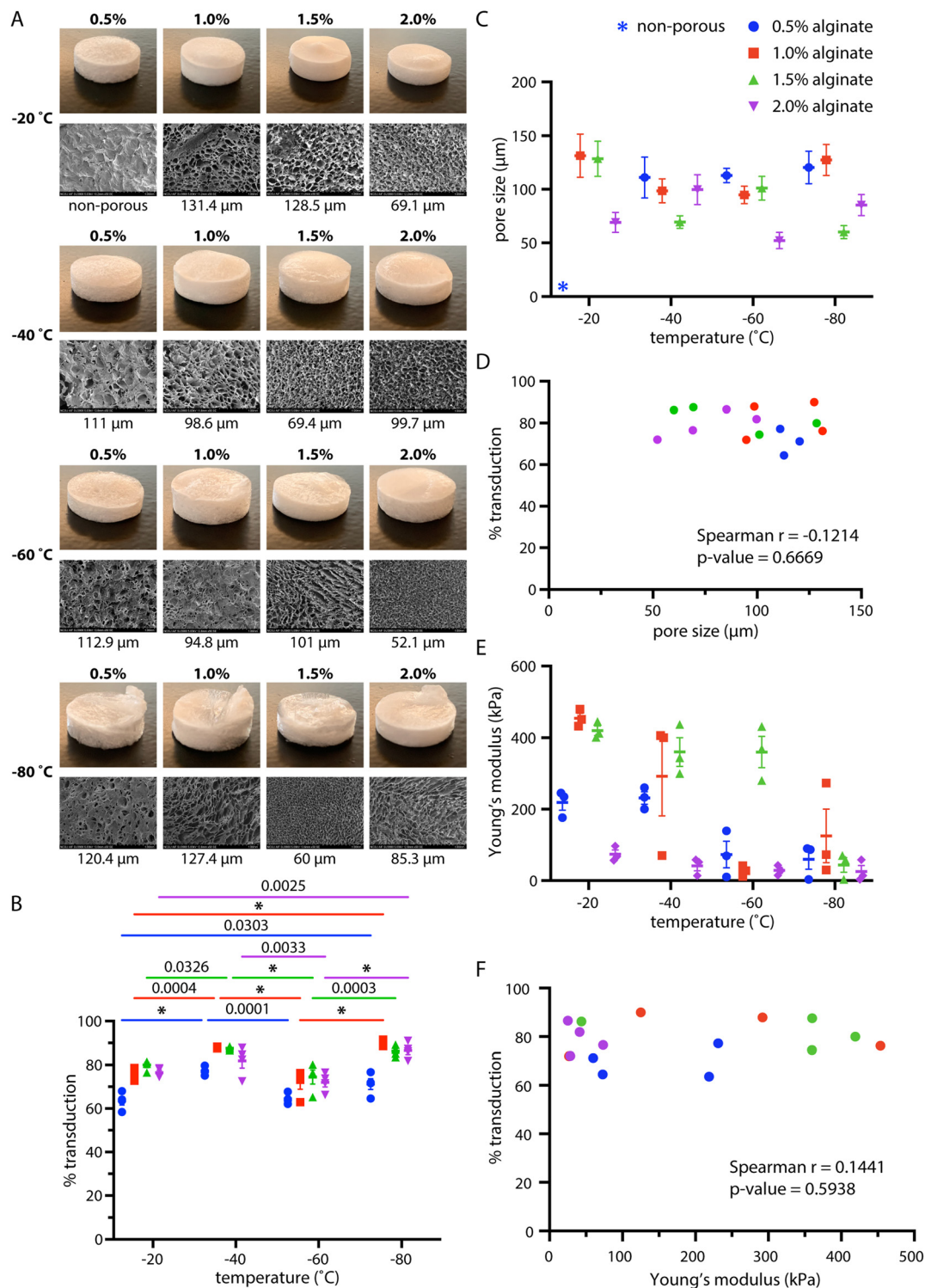


**Fig. 3** Impact of porosity and stiffness on Drydux transduction efficiency varying freezing temperature and alginate concentration. (A) Photographs of scaffolds with corresponding SEM images and average pore sizes. (B) Quantification of retroviral transduction efficiency against primary human T cells for each alginate-temperature combination with significance shown between differing temperatures; \* $p < 0.0001$  with all other  $p$ -values  $< 0.05$  indicated on plot; concentrations used were  $\sim 5000$  cells per  $\mu\text{L}$  and  $\sim 10\,000$  viruses per  $\mu\text{L}$ ;  $n = 3$  scaffolds per group; two-way ANOVA with Tukey correction used to determine significance. See ESI Fig. 4† for significance between differing alginate concentrations. (C) Quantification of scaffold pore size using a minimum of 10 pores per scaffold. (D) Spearman correlation between scaffold pore size and transduction efficiency. (E) Quantification of Young's modulus of each scaffold;  $n = 3$  scaffolds per group. (F) Spearman correlation between scaffold stiffness and transduction efficiency. Data are represented as the mean  $\pm$  SEM. Statistical analysis was not completed for (C) or (E).

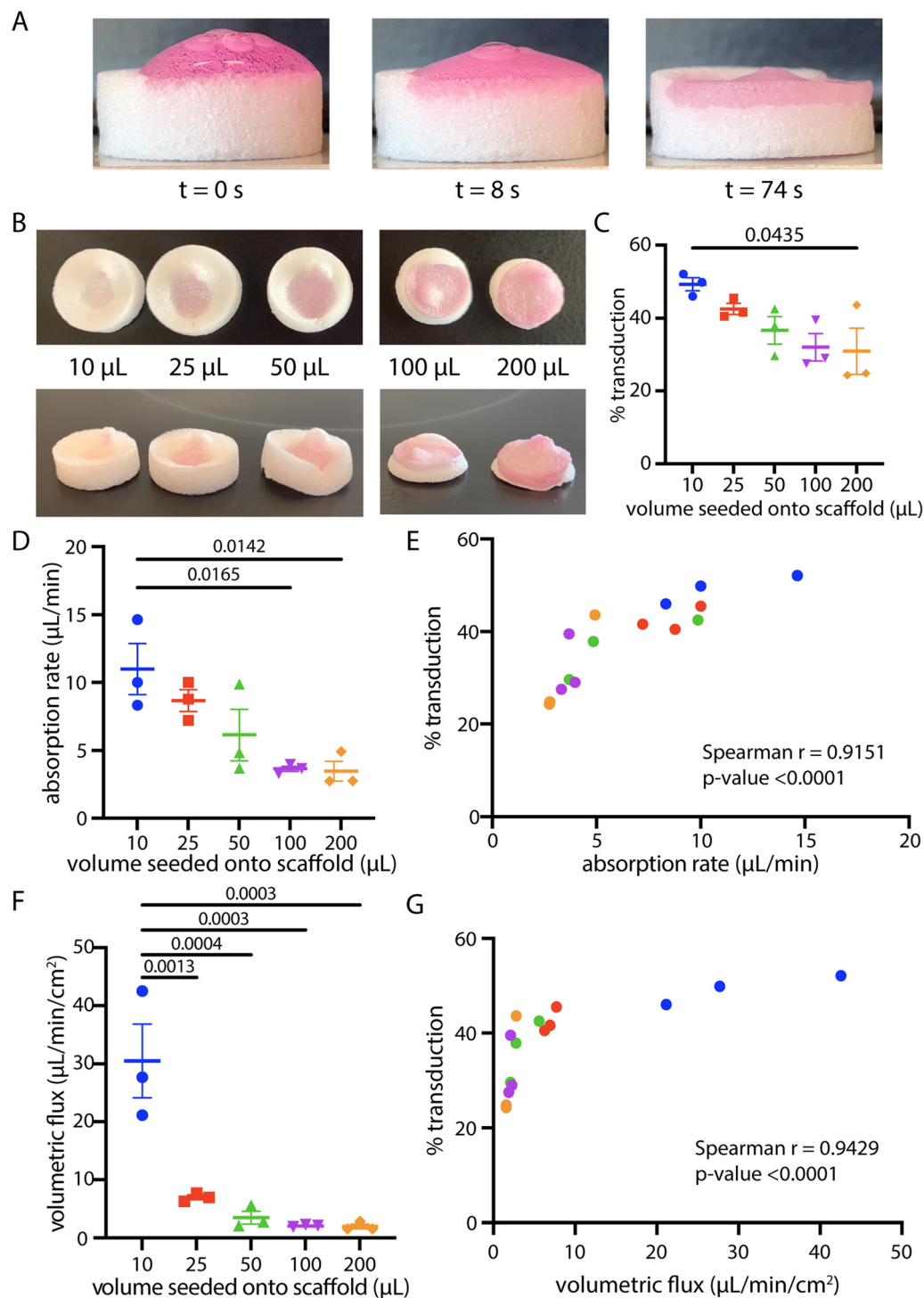


**Fig. 4** Impact of seed volume on Drydux transduction. (A) Live-images of scaffold absorbing 20  $\mu\text{L}$  of cell-virus solution. (B) Images of scaffolds 24 hours after absorbing different volumes of cell-virus solution. (C) Quantification of transduction efficiency for each seed volume. (D) Kinetics of absorption for each seed volume. (E) Spearman correlation between absorption rate and transduction efficiency. (F) Calculated volumetric flux of different seed volumes. (G) Spearman correlation between volumetric flux and transduction efficiency. Data are represented as the mean  $\pm$  SEM; concentrations used were  $\sim$ 2000 cells per  $\mu\text{L}$  and  $\sim$ 4000 viruses per  $\mu\text{L}$ ;  $n = 3$  scaffolds per group; one-way ANOVA was used to determine significance.

primary human T cells and 16 000 particles per  $\mu\text{L}$  retrovirus particles (MOI = 4) onto the scaffold by either spreading the volume around the entire surface area or by seeding the

volume in a single location [ESI Fig. 7A†]. As expected, liquid spread across the whole surface of the scaffold was absorbed faster and produced significantly higher transduction efficien-

cies than the same volume added in a single location of the scaffold [ESI Fig. 7B†]. These results confirm that scaffold surface area can be used to control the absorption rate of the cell–virus solution to influence Drydux transduction.

### Computational model confirms porous structure is critical to transduction efficiency

The above results suggest that liquid flow through the scaffold during absorption governs Drydux transduction. To better understand the possible mechanism behind this observation, we computationally simulated fluid flow through the scaffold. We hypothesized that liquid flow through the scaffold must increase the number of cell–virus collisions and that higher flow rates lead to a higher probability of collisions, thereby improving transduction [Fig. 5A]. Scaffold flow was simulated in Ansys Fluent v21 using the Discrete Particle Method and Computational Fluid Dynamics. Viruses (radius =  $5 \times 10^{-8}$  m) and cells (radius =  $3.5 \times 10^{-6}$  m) were modeled as hard spheres flowing under three scenarios: stationary fluid, uniform unbounded flow, and flow through a scaffold pore [Fig. 5B]. In accordance with previous data we collected on pore geometry,<sup>11</sup> we modeled the scaffold pore geometry as overlapping and interconnected spheres of radius  $7.5 \times 10^{-5}$  m that are spaced  $1.3 \times 10^{-4}$  m apart center-to-center [Fig. 5B]. Periodic boundaries were applied to a representative elementary volume of the geometry to approximate the numerous pores present in the scaffold. The volumetric flux of the flow was varied (1.5, 3.0, 6.0, and  $30.0 \mu\text{L min}^{-1} \text{cm}^{-2}$ ) to represent the experimental volumetric fluxes of different seed volumes into the scaffold pores as reported in Fig. 4F. The flow solution for a time period of 60 s was computed by numerically solving the incompressible Navier–Stokes equations. The particle trajectories were tracked from an initially random distribution using a one-way coupling with the flow solution since the particles

occupy less than 0.1% of the liquid by volume. The particle model includes drag forces on the cell<sup>38</sup> and virus<sup>39</sup> particles, Brownian diffusion,<sup>40</sup> and lift force under shear.<sup>40</sup> When stationary fluid was modeled, no collisions were observed between viruses and T cells. In addition, no collisions were observed in the case of unbounded flow for a volumetric flux of  $1.5 \mu\text{L min}^{-1} \text{cm}^{-2}$  and a small number of collisions were observed for a volumetric flux of  $30 \mu\text{L min}^{-1} \text{cm}^{-2}$ . However, when modeling flow inside the scaffold pore, the flow velocity was predicted to increase by a factor of 4 inside of the constriction point [Fig. 5C] when compared to the widest section of the pore so that the conservation of mass is satisfied. The increased flow velocity inside the scaffold pore created over a twentyfold increase in the number of collisions between T cells and viruses when compared to the unbounded flow [Fig. 5D]. Furthermore, the number of collisions inside the scaffold pore consistently increased with the volumetric flux. The results highlight the importance of the scaffold geometry in promoting interaction between T cells and viruses during the transduction process.

## Discussion and conclusion

The time-consuming and costly process of creating genetically modified cells, including CAR T cells, begs for faster and cheaper technologies to transduce cells. The results of these studies suggest that dry macroporous alginate (Drydux) scaffolds can improve viral T cell transduction and other hard-to-transduce cells. In this work, we have further elucidated the mechanism behind Drydux scaffold function through a study of the impact of pore size, scaffold stiffness, virus concentration, and absorption volume on transduction efficiency. We demonstrate that scaffold pore size has a complicated effect on

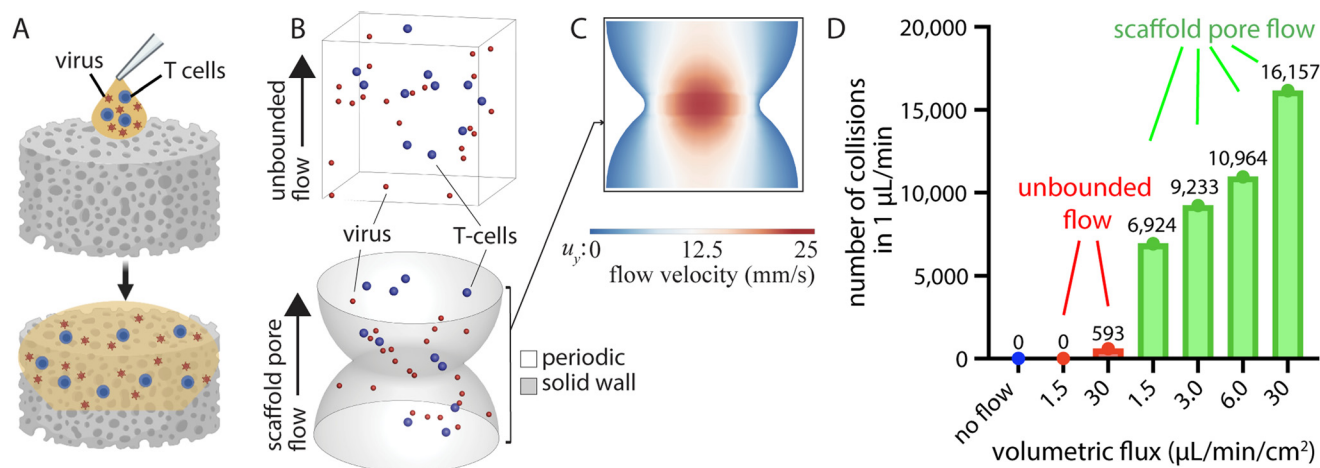


**Fig. 5** Computational model of flow through scaffold pore. (A) Schematic showing activated T cells and virus seeded together onto dry macroporous scaffold. (B) Particle positions at a statistical equilibrium state for uniform unbounded flow (top) and flow inside the scaffold pore at a volumetric flux of  $30 \mu\text{L min}^{-1} \text{cm}^{-2}$  (bottom). (C) The flow velocity distribution at the midplane of the scaffold model showing the flow acceleration and deceleration in response to the changes in the model geometry. (D) Quantification of the number of collisions per  $1 \mu\text{L}$  per minute for no flow, unbounded flow, and scaffold pore flow at different volumetric fluxes.



transduction efficiency and further demonstrate that scaffold stiffness does not impact Drydux transduction. As expected, we discovered that more concentrated virus suspensions led to higher transduction efficiencies, suggesting that in the future cell–virus solution should be as concentrated as possible for optimal transduction efficiency. Interestingly, we found a very strong correlation between absorption speed and transduction efficiency. Finally, we validated these observations using a computational model of cell and virus collisions flowing through a porous scaffold. Based on these results, we propose that absorption speed and volumetric flux are crucial components to Drydux transduction.

From our results, we can conclude scaffold stiffness does not contribute significantly to Drydux transduction. Scaffold stiffness has been shown to effect migration and differentiation of cells within the scaffolds, influencing cell infiltration into host tissues.<sup>41,42</sup> Studies have demonstrated that softer matrices induce higher T cell proliferation and mechanotransduction required for T cell receptor signaling. This is because softer scaffolds usually have higher porosity and interconnectivity, which promotes more interaction among the cells, leading to higher T cell transduction.<sup>22,29,43,44</sup> However, in those examples, scaffold stiffness was altered using adherent cells through cell-adhesion peptides, such as RGD. In the case of Drydux scaffolds, the unmodified alginate does not present adhesion ligands to the T cells, which are themselves non-adhesive cells, likely explaining the lack of impact of scaffold stiffness on Drydux transduction.

The impact of pore size on transduction was somewhat unpredictable. We used SEM imaging to determine pore sizes due to the accessibility and high throughput that SEM imaging provides. However, SEM only provides surface porosity, so future studies could focus on more rigorous pore quantification methods, including microCT, Brunauer–Emmett–Teller (BET) surface area analysis, or porosimetry. We expected that smaller pores would lead to a larger transduction efficiency, as scaffolds with smaller pores usually have a larger porosity and more interconnectivity that allows for greater cell and virus interaction and enhanced diffusion of nutrients and oxygen.<sup>43,44</sup> Although we observed a significant correlation between smaller pore size and transduction when changing the calcium concentration, this correlation disappeared when the pore size was controlled by freezing temperature. We suspect that pore size may still play an important role in cell transduction, but these contradictory results indicate there are other variables at play and further research is required to discern these additional factors.

We discovered that transduction using Drydux scaffolds is likely mediated by the rate of absorption of the cell–virus solution into the scaffold, and our future studies aim to further investigate this hypothesis. The volume of liquid absorbed into the scaffold was inversely proportional to the absorption rate. We suspect this effect is mediated by drag forces of liquid flowing through the interconnected pore structure. Liquid quickly enters the pores due to the hygroscopy of the material. For smaller volumes, the whole volume flows freely without re-

sistance. However, when larger volumes are used, the first volume of liquid absorbed into the scaffold wets the pores and provides drag, impeding the next volume of liquid from freely entering the scaffold and slowing down absorption. The decrease in overall flow rate leads to reduced transduction efficiency.

An alternative explanation for the relationship between volume seeded and transduction efficiency is that liquid absorbs not only into the pores of the scaffold, but also into the walls, decreasing the effective volume and further concentrating cells and virus. Since the final concentration of cells and virus inside the scaffold after absorption is not known, this possibility cannot be excluded. Future studies could investigate the inter-relatedness of liquid absorption, liquid volume, and final cell–virus concentration inside the scaffold.

Sharei *et al.* previously reported that shear stress on cells squeezed through a microfluidic constriction transiently creates holes in the cell membranes, allowing transduction to occur.<sup>45</sup> Although we considered this theory for the Drydux system, the pores are too large to cause this shear stress on the cells. Instead, we believe that transduction is determined by cell–virus collisions due to Brownian motion, fluid convection, and other influences.

In the computational model, interactions between randomly dispersed T cells and viruses are governed by their relative motion. There are four possible sources of relative motion in the flow inside the scaffold: Brownian diffusion, drag forces on the differently sized T cell and virus particles, pressure gradients caused by the pore geometry of the scaffold, and Saffman lift due to shear at the scaffold wall. Since no collisions were observed in a stationary fluid, we believe that Brownian diffusion alone is not sufficient to cause the particles to collide. Substantial increases in the cell–virus collisions was observed only in the case of the flow through the scaffold model. The interconnected pore geometry of the scaffold causes acceleration and deceleration of the flow in the converging and diverging sections of the geometry, respectively. The drag force on the particle is directly related to the velocity difference between the particle and the fluid, which in turn accelerates the particle in response to the acceleration of the fluid. The different laws governing the drag forces acting on the microscale cells and the submicron viruses, along with the inertia of the particles, causes relative motion between the virus and cell particles. In addition, the highest particle flux is experienced near the constriction point in the scaffold pore, which has the smallest cross-section area. For a volumetric flux of  $30 \mu\text{L min}^{-1} \text{cm}^{-2}$ , the particle flux at the constriction point is 2.8 times higher than at the widest section. In this case, over 75% of the collisions take place in the converging section of the scaffold pore.

One promising conclusion from these studies is that Drydux transduction is a robust process that remained efficient across a wide array of alginate concentrations, calcium concentrations, and freezing temperatures. The robust nature of the system gives more credence to the possibility that Drydux scaffolds can find utility in the production of cellular therapies and specifically benefit CAR T cell therapies for solid

tumors, where tuning scaffold mechanics to the mechanics of the surrounding tissue could improve the success of treatment. This becomes highly important when treating specific solid tumors, such as glioblastoma, where matching the scaffold stiffness to that of the brain can effect cell viability, migration, and infiltration into surrounding tissues.<sup>41,42</sup>

## Conflicts of interest

Y. B. is an inventor on patents related to the use of biomaterials for generation of CAR-T cell therapeutics and receives an industry-sponsored research grant related to CAR-T cell therapeutic technology (unrelated to this work). All other authors declare that they have no competing interests.

## Acknowledgements

This work was supported by the National Institutes of Health through Grant Award Numbers R37-CA260223, R21-CA246414. We thank the NCSU flow cytometry core for training and guidance on flow cytometry analysis. We thank Zachary Davis for training and guidance on the Instron 5944. Schematics were created with Biorender.com. SEM images were provided by the Analytical Instrumentation Facility (AIF) at North Carolina State University, which is supported by the State of North Carolina and the National Science Foundation (ECCS-1542015). The AIF is a member of the North Carolina Research Triangle Nanotechnology Network (RTNN), a site in the National Nanotechnology Coordinated Infrastructure (NNCI). Computing resources were provided by North Carolina State University High Performance Computing Services Core Facility (RRID: SCR\_022168). AVK acknowledges the support of the National Science Foundation (award CBET-2042834) and the Alexander Humboldt Foundation Research Award. GFP-encoding retrovirus producer cell lines were generously provided by the Dotti lab at the University of North Carolina.

## References

- 1 J. K. Kim, H. J. Kim, J.-Y. Chung, J.-H. Lee, S.-B. Young and Y.-H. Kim, Natural and Synthetic Biomaterials for Controlled Drug Delivery, *Arch. Pharmacol. Res.*, 2014, **37**(1), 60–68.
- 2 M. S. Hamid Akash, K. Rehman and S. Chen, Natural and Synthetic Polymers as Drug Carriers for Delivery of Therapeutic Proteins, *Polym. Rev.*, 2015, **55**(3), 371–406.
- 3 J. Sun and H. Tan, Alginate-Based Biomaterials for Regenerative Medicine Applications, *Materials*, 2013, **6**(4), 1285–1309.
- 4 I. Safina and M. C. Embree, Biomaterials for Recruiting and Activating Endogenous Stem Cells in Situ Tissue Regeneration, *Acta Biomater.*, 2022, **143**, 26–38.
- 5 S. S. Soni and C. B. Rodell, Polymeric Materials for Immune Engineering: Molecular Interaction to Biomaterial Design, *Acta Biomater.*, 2021, **133**, 139–152.
- 6 C. J. Bashor, I. B. Hilton, H. Bandukwala, D. M. Smith and O. Veisoh, Engineering the next Generation of Cell-Based Therapeutics, *Nat. Rev. Drug Discovery*, 2022, **21**(9), 655–675.
- 7 H.-R. Lin and Y.-J. Yeh, Porous Alginate/Hydroxyapatite Composite Scaffolds for Bone Tissue Engineering: Preparation, Characterization, And In Vitro Studies, *J. Biomed. Mater. Res.*, 2004, 52–65, DOI: [10.1002/jbm.b.30065](https://doi.org/10.1002/jbm.b.30065).
- 8 R. Guo, Y. Zhou, S. Liu, C. Li, C. Lu, G. Yang, J. Nie, F. Wang, N.-G. Dong and J. Shi, Anticalcification Potential of POSS-PEG Hybrid Hydrogel as a Scaffold Material for the Development of Synthetic Heart Valve Leaflets, *ACS Appl. Bio Mater.*, 2021, **4**(3), 2534–2543.
- 9 C. T. Moody, S. Palvai and Y. Brudno, Click Cross-Linking Improves Retention and Targeting of Refillable Alginate Depots, *Acta Biomater.*, 2020, **112**, 112–121.
- 10 Y. Brudno, M. J. Pezone, T. K. Snyder, O. Uzun, C. T. Moody, M. Aizenberg and D. J. Mooney, Replenishable Drug Depot to Combat Post-Resection Cancer Recurrence, *Biomaterials*, 2018, **178**, 373–382.
- 11 P. Agarwalla, E. A. Ogunnaike, S. Ahn, K. A. Froehlich, A. Jansson, F. S. Ligler, G. Dotti and Y. Brudno, Bioinstructive Implantable Scaffolds for Rapid in Vivo Manufacture and Release of CAR-T Cells, *Nat. Biotechnol.*, 2022, **40**, 1250–1258.
- 12 K. M. Moore, E. G. Graham-Gurysh, H. N. Bomba, A. B. Murthy, E. M. Bachelder, S. D. Hingtgen and K. M. Ainslie, Impact of Composite Scaffold Degradation Rate on Neural Stem Cell Persistence in the Glioblastoma Surgical Resection Cavity, *Mater. Sci. Eng., C*, 2020, **111**, 110846.
- 13 A. K. Nayak, B. C. Mohanta, M. S. Hasnain, M. N. Hoda and G. Tripathi, Alginate-Based Scaffolds for Drug Delivery in Tissue Engineering, in *Alginates in Drug Delivery*, ed. A. K. Nayak and M. S. Hasnain, Academic Press, 2020, ch. 14, pp. 359–386.
- 14 K. Y. Lee and D. J. Mooney, Alginate: Properties and Biomedical Applications, *Prog. Polym. Sci.*, 2012, **37**(1), 106–126.
- 15 C. K. Kuo and P. X. Ma, Ionically Crosslinked Alginate Hydrogels as Scaffolds for Tissue Engineering: Part 1. Structure, Gelation Rate and Mechanical Properties, *Biomaterials*, 2001, **22**(6), 511–521.
- 16 C. Soccol, J. De Dea, C. Yamaguishi, M. Spier, L. de Souza and V. Soccol, Probiotic Nondairy Beverages, *Handbook of Plant-Based Fermented Food and Beverage Technology*, 2nd edn, 2012, pp. 707–728. DOI: [10.1201/b12055-51](https://doi.org/10.1201/b12055-51).
- 17 B. L. Prinzing, S. M. Gottschalk and G. Krenciute, CAR T-Cell Therapy for Glioblastoma: Ready for the next Round of Clinical Testing?, *Expert Rev. Anticancer Ther.*, 2018, **18**(5), 451–461.
- 18 S. J. Bagley, A. S. Desai, G. P. Linette, C. H. June and D. M. O'Rourke, CAR T-Cell Therapy for Glioblastoma: Recent Clinical Advances and Future Challenges, *Neuro-Oncology*, 2018, **20**(11), 1429–1438.

- 19 R. Nair and J. Westin, CAR T Cells, *Adv. Exp. Med. Biol.*, 2021, 297–317, DOI: [10.1007/978-3-030-79308-1\\_10](https://doi.org/10.1007/978-3-030-79308-1_10).
- 20 H. J. Jackson, S. Rafiq and R. J. Brentjens, Driving CAR T-Cells Forward, *Nat. Rev. Clin. Oncol.*, 2016, **13**(6), 370–383.
- 21 R. C. Sterner and R. M. Sterner, CAR-T Cell Therapy: Current Limitations and Potential Strategies, *Blood Cancer J.*, 2021, **11**(4), 69.
- 22 I. I. Cardle, E. L. Cheng, M. C. Jensen and S. H. Pun, Biomaterials in Chimeric Antigen Receptor T-Cell Process Development, *Acc. Chem. Res.*, 2020, **53**(9), 1724–1738.
- 23 R. S. O'Connor, X. Hao, K. Shen, K. Bashour, T. Akimova, W. W. Hancock, L. C. Kam and M. C. Milone, Substrate Rigidity Regulates Human T Cell Activation and Proliferation, *J. Immunol.*, 2012, **189**, 1330–1339.
- 24 J. Matic, J. Deeg, A. Scheffold, I. Goldstein and J. P. Spatz, Fine Tuning and Efficient T Cell Activation with Stimulatory ACD3 Nanoarrays, *Nano Lett.*, 2013, **13**(11), 5090–5097.
- 25 S. B. Stephan, A. M. Taber, I. Jileeva, E. P. Pegues, C. L. Sentman and M. T. Stephan, Biopolymer Implants Enhance the Efficacy of Adoptive T-Cell Therapy, *Nat. Biotechnol.*, 2015, **33**(1), 97–101.
- 26 P. Agarwalla, E. A. Ogunnaike, S. Ahn, F. S. Ligler, G. Dotti and Y. Brudno, Scaffold-Mediated Static Transduction of T Cells for CAR-T Cell Therapy, *Adv. Healthcare Mater.*, 2020, **9**(14), e2000275.
- 27 T. T. Smith, S. B. Stephan, H. F. Moffett, L. E. McKnight, W. Ji, D. Reiman, E. Bonagofski, M. E. Wohlfahrt, S. P. S. Pillai and M. T. Stephan, In Situ Programming of Leukaemia-Specific T Cells Using Synthetic DNA Nanocarriers, *Nat. Nanotechnol.*, 2017, **12**(8), 813–820.
- 28 T. T. Smith, H. F. Moffett, S. B. Stephan, C. F. Opel, A. G. Dumigan, X. Jiang, V. G. Pillarisetty, S. P. S. Pillai, K. D. Wittrup and M. T. Stephan, Biopolymers Codelivering Engineered T Cells and STING Agonists Can Eliminate Heterogeneous Tumors, *J. Clin. Invest.*, 2017, **127**(6), 2176–2191.
- 29 J. Weiden, D. Voerman, Y. Dölen, R. K. Das, A. van Duffelen, R. Hammink, L. J. Eggermont, A. E. Rowan, J. Tel and C. G. Figdor, Injectable Biomimetic Hydrogels as Tools for Efficient T Cell Expansion and Delivery, *Front. Immunol.*, 2018, **9**, 2798.
- 30 A. S. Cheung, D. K. Y. Zhang, S. T. Koshy and D. J. Mooney, Scaffolds That Mimic Antigen-Presenting Cells Enable Ex Vivo Expansion of Primary T Cells, *Nat. Biotechnol.*, 2018, **36**(2), 160–169.
- 31 H.-J. Lee, Y.-S. Lee, H.-S. Kim, Y.-K. Kim, J.-H. Kim, S.-H. Jeon, H.-W. Lee, S. Kim, H. Miyoshi, H.-M. Chung and D.-K. Kim, Retronectin Enhances Lentivirus-Mediated Gene Delivery into Hematopoietic Progenitor Cells, *Biologicals*, 2009, **37**(4), 203–209.
- 32 A. Rajabzadeh, A. A. Hamidieh and F. Rahbarizadeh, Spinoculation and Retronectin Highly Enhance the Gene Transduction Efficiency of Mucin-1-Specific Chimeric Antigen Receptor (CAR) in Human Primary T Cells, *BMC Mol. Cell Biol.*, 2021, **22**(1), 57.
- 33 M. VanBlunk, P. Agarwalla, S. Pandit and Y. Brudno, Fabrication and Use of Dry Macroporous Alginate Scaffolds for Viral Transduction of T Cells, *J. Visualized Exp.*, 2022, **187**, DOI: [10.3791/64036](https://doi.org/10.3791/64036).
- 34 The University of Texas MD Anderson Cancer Center, Protocol for Virus titer by flow cytometry, <https://www.mdanderson.org/documents/core-facilities/Functional%20Genomics%20Core/Virus%20titration%20protocols.pdf>.
- 35 F. Carpi, I. Anderson, S. Bauer, G. Frediani, G. Gallone, M. Gei, C. Graaf, C. Jean-Mistral, W. Kaal, G. Kofod, M. Kollosche, R. Kornbluh, B. Lassen, M. Matysek, S. Michel, S. Nowak, B. O'Brien, Q. Pei, R. Pelrine, B. Rechenbach, S. Rosset and H. Shea, Standards for Dielectric Elastomer Transducers, *Smart Mater. Struct.*, 2015, **24**(10), 105025.
- 36 I. Diaconu, B. Ballard, M. Zhang, Y. Chen, J. West, G. Dotti and B. Savoldo, Inducible Caspase-9 Selectively Modulates the Toxicities of CD19-Specific Chimeric Antigen Receptor-Modified T Cells, *Mol. Ther.*, 2017, **25**(3), 580–592.
- 37 J. Wu, Q. Zhao, J. Sun and Q. Zhou, Preparation of Poly (Ethylene Glycol) Aligned Porous Cryogels Using a Unidirectional Freezing Technique, *Soft Matter*, 2012, 3620, DOI: [10.1039/c2sm07411g](https://doi.org/10.1039/c2sm07411g).
- 38 S. A. Morsi and A. J. Alexander, An Investigation of Particle Trajectories in Two-Phase Flow Systems, *J. Fluid Mech.*, 1972, **55**(2), 193–208.
- 39 H. Ounis, G. Ahmadi and J. B. McLaughlin, Brownian Diffusion of Submicrometer Particles in the Viscous Sublayer, *J. Colloid Interface Sci.*, 1991, **143**(1), 266–277.
- 40 A. Li and G. Ahmadi, Dispersion and Deposition of Spherical Particles from Point Sources in a Turbulent Channel Flow, *Aerosol Sci. Technol.*, 1992, **16**(4), 209–226.
- 41 R. G. M. Breuls, T. U. Jiya and T. H. Smit, Scaffold Stiffness Influences Cell Behavior: Opportunities for Skeletal Tissue Engineering, *Open Orthop. J.*, 2008, 103–109, DOI: [10.2174/1874325000802010103](https://doi.org/10.2174/1874325000802010103).
- 42 J. Bruns, T. Egan, P. Mercier and S. P. Zusiak, Glioblastoma Spheroid Growth and Chemotherapeutic Responses in Single and Dual-Stiffness Hydrogels, *Acta Biomater.*, 2022, **22**, S1742–7061.
- 43 N. Annabi, J. W. Nichol, X. Zhong, C. Ji, S. Koshy, A. Khademhosseini and F. Dehghani, Controlling the Porosity and Microarchitecture of Hydrogels for Tissue Engineering, *Tissue Eng., Part B*, 2010, **16**(4), 371–383.
- 44 C. M. Hwang, S. Sant, M. Masaeli, N. N. Kachouie, B. Zamanian, S.-H. Lee and A. Khademhosseini, Fabrication of Three-Dimensional Porous Cell-Laden Hydrogel for Tissue Engineering, *Biofabrication*, 2010, **2**(3), 035003.
- 45 A. Sharei, J. Zoldan, A. Adamo, W. Y. Sim, N. Cho, E. Jackson, S. Mao, S. Schneider, M.-J. Han, A. Lytton-Jean, P. A. Basto, S. Jhunjhunwala, J. Lee, D. A. Heller, J. W. Kang, G. C. Hartoularos, K.-S. Kim, D. G. Anderson, R. Langer and K. F. Jensen, A Vector-Free Microfluidic Platform for Intracellular Delivery, *Proc. Natl. Acad. Sci. U. S. A.*, 2013, **110**(6), 2082–2087.